Supporting Information

The Role of Oxygen in Automotive Grade Lithium-Ion Battery Cathodes: An Atomistic Survey of Ageing

Anastasiia Mikheenkova[a], Soham Mukherjee[b], Moritz Hirsbrunner[b], Pontus Törnblom[b], Cheuk-Wai Tai[c], Carlo U. Segre[d], Yujia Ding[d], Wenliang Zhang[e], Teguh Citra Asmara[e], Yuan Wei[e], Thorsten Schmitt[e], Håkan Rensmo[b], Laurent Duda[b], and Maria Hahlin[a,b,*]*

[a] *Ångström Laboratory, Department of Chemistry, Uppsala University, SE 751 21 Uppsala, Sweden.*

[b] *Ångström Laboratory, Department of Physics and Astronomy, Uppsala University, SE 751 21 Uppsala, Sweden.*

[c] *Department of Materials and Environmental Chemistry, Arrhenius Laboratory, Stockholm University, Stockholm, 10691 Sweden.*

[d] *Department of Physics and CSRRI, Illinois Institute of Technology, Chicago, IL 60616, USA.*

[e] *Laboratory for condensed matter, Paul Scherrer Institute, Forschungsstrasse 111, Villigen PSI, 5232, Switzerland.*

[*] *Corresponding author.*

E-mail: maria.hahlin@kemi.uu.se

Table of Contents

Experimental

Materials

Commercial 2170 cylindrical cells, pouch material (Skilstuna Flexible, predried at 60° C in an oven), 1 mol/L lithium hexafluorophosphate dissolved in 1:1 v/v Ethylene carbonate

: Diethyl carbonate (LP40, 1 M $LiPF_6$ in 1:1 EC:DEC, Solvionic, was used as received), Celgard 2325 (Celgard, cleaned with ethanol, deionized water and dried in Buchi oven at 60° C for 12 hours), Li (MTI Corporation, thickness 450 μm, used as received).

Cell tear-down

Commercial 2170 cylindrical cells were extracted from Tesla Model 3 battery pack. Part of the cells were taken apart and considered as Beginning of Life (BoL). The rest of the cells were aged at 45° C between 0-50 % SoC and 0-100 % SoC. The End of Life (EoL) was considered when the cell experienced 25% loss of initial capacity. The samples are specified in Table S 1. Full cycle equivalent (FCE) corresponds to the number of cycles done by full cell during ageing. Positive electrode (PE) capacity loss was measured and presented in the previous study.[1]The BoL and EoL electrodes from the same cells were used in the previous studies.[2]

Table S 1: Sample matrix describing the sample names and corresponding cell ageing conditions. Adapted from[2]

Sample	**Ageing condition**	**FCE**	**dQ,%**	**LAM**
Aged L	0-50 %SoC	950	20.84	-17 ± 3.2 %
Aged H	0-100 %SoC	1050	19.76	-23 ± 6.9 %

After reaching end of life the cells were discharged to 0% SoC and were opened in an Ar filled glove-box.

Sample preparation for *in situ* measurements

The extracted electrodes were cleaned from one side of coating using scalpel and punched with a diameter 8 mm. The assembled pouch cell consisted of NCA as PE, Li as counter

electrode, Celgard 2325 as a separator and LP40 was used as electrolyte.

For *in-situ* electrode preparation, Arbin and Biologic cycling equipment were used. The set of samples corresponding to 2.55 V, 3.60 V, and 4.20 V vs Li/Li^+ was prepared by discharging assembled half cells to 2.55 V first and then cycled with a constant current 50 μA until reaching desired potential. After that, the constant current was followed by constant voltage step for 4 h until the current was lower then C/50. After, the cells were disassembled in Ar filled glovebox and the electrodes were cut in halves. 2 mm stripe was cut from every electrode for RIXS studies and the other part was used for the XAS studies.

RIXS/Soft XAS

High resolution XAS and RIXS spectra of the oxygen K- and nickel $L_{2,3}$-edges were obtained at the soft X-ray beamline ADRESS at the SLS, Villigen-PSI, Switzerland. XAS spectra were obtained in total fluorescence yield (TFY) mode. RIXS measurements were conducted using the VLS spherical grating based Super Advanced X-ray Emission Spectrometer (SAXES) allowing for an energy range of 0.3 keV - 1.6 keV and a resolution of 10000, i.e. 50 meV at 500 eV. RIXS and XAS data presented in subsection "Ni and Co charge compensation mechanisms and its change with ageing" is taken from the same dataset.

Additionally, RIXS of Li rich $Li[Li_{0.2}Ni_{0.13}Co_{0.13}Mn_{0.54}]O_2$ (from here on shortened to Li-rich NMC) was also measured as a reference to compare the extent of the O_2 formation with the NCA.

Hard XAS/EXAFS

K-edge XAS data for Co and Ni were collected at the Materials Research Collaborative Team (MRCAT) Sector 10-ID line of the Advanced Photon Source, Argonne National Laboratory

(aged electrodes) and the P64 beamline, DESY, Hamburg (fresh electrodes), utilizing high photon flux on the sample ($\sim 10^{12}$ photons/sec at 8 keV) and high resolution ($\Delta E/E \approx 10^{-4}$). At the APS, a Si (111) double crystal monochromator detuned by 50% to remove higher harmonics, was used to monochromatize the incident photon beam. A mixture of N_2 and He gas was optimized in the ion-chambers to absorb ~5-10% of the incident photons. The electrodes were mounted to the sample holder and oriented at 45 degrees with respect to the incoming x-ray beam, allowing simultaneous measurements in transmission and fluorescence geometry. An identical N_2:He gas mixture was used for transmission measurements, as well as the reference channel where the respective metal foils were mounted (Co or Ni) to track for any undesired energy drifts. Fluorescence data were collected by using a 4-element Vortex (Hitachi) SDD detector with xMap (XiA) digital pulse processing electronics. Similar XAS measurements on Ni and Co *K*-edges for the fresh electrodes were performed at P64, DESY using a Si (111) double-crystal monochromator without detuning and using N_2 in the ion-chambers. Fluorescence data were collected simultaneously using a Passivated Implanted Planar Silicon (PIPS) detector (Canberra). Significant statistics were collected for both Ni and Co for each sample. The Co *K*-edge XAS data range is limited by the presence of Ni, limiting the usable *k* range to $\approx$ 12 Å^1, while Ni *K*- XAS could be collected up to *k* range to $\approx$ 15 Å^1. All XAS data sets were processed and analyzed using Athena-Artemis software suite, a front end to FEFF and IFEFFIT.[3] The subtracted background was calculated using AUTOBK algorithm implemented in the software.[4] The errors were estimated by a standard Levenberg-Marquardt, non-linear minimization of the statistical χ^2 parameter, built within the FEFF6 program. Fits to all Ni and Co data in *R* (real part and magnitude) and *q*-spaces, extracted EXAFS parameters and their associated error limits are detailed in the Supporting Information.

TEM

TEM lamellae were prepared using a Focused Ion Beam (FIB), model Crossbeam 550 (Zeiss). The surface of the sample was protected with a carbon and a Pt layer and the polishing procedure was completed using a 2 kV ion accelerating voltage to limit residual damages in the final sample. The STEM study was carried out in a double aberration-corrected Themis Z (Thermo Fisher). The microscope was operated at 300 kV and equipped with a Super-X EDS detector. The aberrations in the condenser lens system were corrected up to 5^{th} order. The convergence angle of 21 mrad and probe current of 120 pA were applied for imaging and EDS analysis. The collection angle of HAADF- and BF-STEM images were 63-200 mrad and below 35 mrad, respectively. Imaging and EDS acquisition and analysis were performed using Thermo Fisher Velox.

SEM

The scanning electron microscopy (SEM) study was done using SEMA Zeiss LEO 1530. SEM with InLens detector was performed using an acceleration voltage of 5 kV and a working distance of 6.5 mm.

EXAFS analyses

Data reduction

The XAS data were first converted to absorption versus energy and calibrated in energy to the reference channels. The background in the pre-edge region was accounted for using a linear fit, and the background in the energy region $>$ 150 eV beyond the E_0 position was accounted for using a spline function (cubic). All the transmission spectra were normalized to have an edge-step of 1. The EXAFS oscillations ($\chi(k)$) were extracted from the higher energy region of the XAS spectra and eventually Fourier transformed into real space

($\chi(R)$) information. The amplitude reduction factor ($S_0{}^2$) values for Ni and Co were extracted individually which yielded similar values, so an average value single value, which was 0.7 for Ni and 0.85 for Co, was assigned to the respective data sets and retained as constant values for all the fits. Coordination numbers, bond distances, energy offsets, pseudo-Debye-Waller factors (σ^2) were extracted as local structural parameters. Since interference from Ni *K*- edge limits the Co *k* range beyond $\approx$ 12.0 Å^{-1}, we used same k-range fit both Ni and Co data sets. Choosing identical *k* and *R*-ranges allow for a proper comparison of Ni and Co by minimizing any bias on the fits, as the resolution of EXAFS strongly depends on these ranges ($\approx 2\Delta k \Delta R/\pi$). An identical Hanning window (Δk = 2 Å^{-1}, ΔR = 0.2 Å) used for all Ni and Co data fits.

First shell fits

The fit range employed was 2.0 – 11.0 Å^{-1} in *k*-space and 1.0-2.2 Åin *R*-space. This allows estimation of $\approx$ 7 independent parameters, which could easily track whether the Ni-O or Co-O bonds are strong distorted within the O_6 octahedra. The EXAFS pattern was calculated for $LiNiCoAlO_2$ from the available crystal structure information in the Inorganic Crystal Structure Data-base ICSD-1533585) as the starting model, with Ni being the central atom. Two second calculations were performed, where the neighbouring Ni atoms were replaced by Co and Al. All three calculations were used while fitting the higher shell of Ni *K*-data. For Co *K*-, same method was adopted, the central atoms being defined as Co. Modeling 1NN (first near neighbor) with a single TM-O (Ni or Co) bond gave good fit quality, with R factors as low as 0.2%.

Including a second TM-O bond improves the fit slightly, but underestimates the σ^2 values. A third TM-O bond destabilizes the model, with two TM-O distances being identical with high uncertainties, and a much shorter TM-O bond ($\approx$ 0.5 Å), which is an unphysical solution. Also, the 1 TM-O bond model was much more stable during simultaneous fitting

of all Ni or Co data. The 1NN environment description, therefore was best captured by a single TM-O bond with structural distortions occurring withing the O_6 cage during the lithiation-delithiation defined in terms of σ^2.

Higher shell fits

A larger *R*-range up to 3.3 Åwas chosen to capture the second EXAFS peak. This peak is dominated by Co and Ni, less by Al, with almost no contribution from Li. Co and Ni have very similar are scattering factors, so the ratio of the metal sites was defined from the nominal composition ratio with just one free parameter. Apart from the metal-metal direct scattering paths, two more paths were found to be significant contributors to the EXAFS: one single scattering from next nearest O and one double scattering -O-TM- path. All the higher shell paths were modeled using a single expansion factor. For the final fits, O-coordination numbers were fixed to 6, and coordination numbers for higher shell paths were estimated using the free parameter multiplied by their respective coordination numbers given by the crystal structure. The expansion factors were eventually converted to bond distances and tabulated (Table S 2).

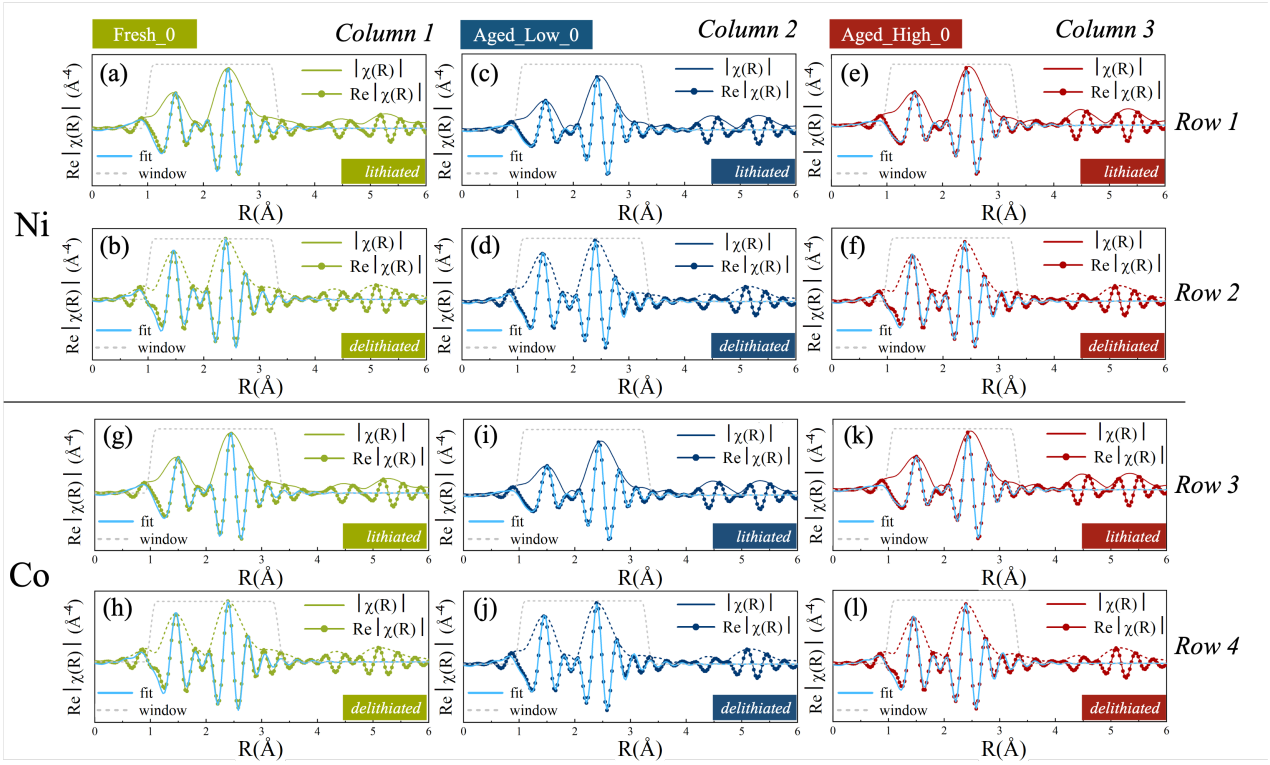

Figure S 1: Fits to real part of $\chi(R)$ with corresponding modulus of $\chi(R)$ for Ni (Rows 1,2) and Co (Rows 3,4) EXAFS for fresh (column 1) and aged electrodes 0-50% SoC (column 2 column) and 0-100% SoC (column 3).

Table S 2: Ni and Co K- EXAFS fit parameters: interatomic distances (*R*), pseudo Debye-Waller factors (σ^2), coordination numbers (*N*), amplitudes (*amp*) energy shift parameters (Δ E_0) and *R*-factor values representing the quality of the fit.

Fresh 0							
Ni	Scattering atom	R (Å)	σ^2 (Å^2)	N	amp	ΔE_0 (eV)	*R*-factor
	O	1.93±0.01	0.0095 ±0.0011	6	-	-9.7±1.4	0.015
	TM	2.858±0.007	0.0048±7.4x10^{-4}	6	1.0±0.1		
	Li	2.883±0.007	0.01	6			
	O-Al	3.386±0.008		24			
	O	3.464±0.009		6			
Co	Scattering atom	R (Å)	σ^2 (Å^2)	N	amp	ΔE_0 (eV)	*R*-factor
	O	1.906±0.008	0.0023±7.1x10^{-4}	6	-	-5.9±1.6	0.016
	TM	2.841±0.008	0.0021±5.5x10^{-4}	6	1.01±0.07		
	Li	2.867±0.008	0.00965	6			
	O-Al	3.367±0.009		24			
	O	3.445±0.009		6			

Fresh 100							
Ni	Scattering atom	*R*(Å)	σ^2 (Å^2)	N	amp	ΔE_0 (eV)	*R*-factor
	O	1.885±0.007	0.0044 ±9.0x10^{-4}	6	-	-9.7±1.4	0.031
	TM	2.812±0.004	0.0035±4.9x10^{-4}	6	1.0±0.02		
	Li	2.838±0.004	0.01	6			
	O-Al	3.332±0.005		24			
	O	3.409±0.005		6			
Co	Scattering atom	*R*(Å)	σ^2 (Å^2)	N	amp	ΔE_0 (eV)	*R*-factor
	O	1.89±0.01	0.0028±0.001	6	-	-6.3±2.1	0.028
	TM	2.814±0.01	0.0017±6.4x10^{-4}	6	1.0±0.07		
	Li	2.84±0.01	0.00965	6			
	O-Al	3.33±0.01		24			
	O	3.41±0.01		6			

Aged L 0							
	Scattering atom	R(Å)	σ^2 (Å^2)	N	amp	ΔE_0 (eV)	R-factor
Ni	O	1.952±0.007	0.01±7.1x10^{-4}	6	-	-5.4±0.8	0.005
	TM	2.868±0.004	0.0041±4.1x10^{-4}	6	0.99±0.06		
	Li	2.894±0.004	0.01	6			
	O-Al	3.399±0.005		24			
	O	3.477±0.005		6			
	Scattering atom	R(Å)	σ^2 (Å^2)	N	amp	ΔE_0 (eV)	R-factor
Co	O	1.914±0.005	0.0036±4.0x10^{-4}	6	-	-6.6±0.9	0.006
	TM	2.857±0.005	0.0042±5.1x10^{-4}	6	1.03±0.07		
	Li	2.883±0.005	0.00965	6			
	O-Al	3.385±0.006		24			
	O	3.463±0.006		6			

Aged L 100							
	Scattering atom	R(Å)	σ^2 (Å^2)	N	amp	ΔE_0 (eV)	R-factor
Ni	O	1.887±0.005	0.0046±4.9x10^{-4}	6	-	-8.2±0.9	0.007
	TM	2.82±0.005	0.0036±4.8x10^{-4}	6	1.04±0.07		
	Li	2.845±0.005	0.01	6			
	O-Al	3.341±0.005		24			
	O	3.418±0.006		6			
	Scattering atom	R(Å)	σ^2 (Å^2)	N	amp	ΔE_0 (eV)	R-factor
Co	O	1.888±0.006	0.0033±5.3x10^{-4}	6	-	-8.1±1.2	0.011
	TM	2.813±0.006	0.0036±8.6x10^{-4}	6	1.0±0.1		
	Li	2.839±0.006	0.00965	6			
	O-Al	3.333±0.007		24			
	O	3.41±0.007		6			

Aged H 0							
Ni	Scattering atom	R(Å)	σ^2 (Å^2)	N	amp	ΔE_0 (eV)	R-factor
	O	1.948±0.008	0.0083±8.6x10^{-4}	6	-	-4.7±1.0	0.008
	TM	2.868±0.005	0.0038±5.1x10^{-4}	6	1.07±0.08		
	Li	2.894±0.005	0.01	6			
	O-Al	3.398±0.006		24			
	O	3.477±0.007		6			
Co	Scattering atom	R(Å)	σ^2 (Å^2)	N	amp	ΔE_0 (eV)	R-factor
	O	1.914±0.005	0.0034±3.9x10^{-4}	6	-	-6.2±0.9	0.006
	TM	2.856±0.004	0.0039±4.8x10^{-4}	6	1.02±0.07		
	Li	2.882±0.005	0.00965	6			
	O-Al	3.384±0.005		24			
	O	3.462±0.005		6			

Aged H 100							
Ni	Scattering atom	R(Å)	σ^2 (Å^2)	N	amp	ΔE_0 (eV)	R-factor
	O	1.886±0.008	0.005±7.8x10^{-4}	6	-	-8.2±1.4	0.017
	TM	2.814±0.007	0.0034±5.4x10^{-4}	6	0.99±0.06		
	Li	2.84±0.007	0.01	6			
	O-Al	3.335±0.008		24			
	O	3.412±0.008		6			
Co	Scattering atom	R(Å)	σ^2 (Å^2)	N	amp	ΔE_0 (eV)	R-factor
	O	1.887±0.006	0.0032±5.6x10^{-4}	6	-	-8.0±1.3	0.011
	TM	2.811±0.006	0.0032±8.4x10^{-4}	6	0.99±0.1		
	Li	2.837±0.006	0.00965	6			
	O-Al	3.331±0.007		24			
	O	3.408±0.008		6			

Sample preparation

The sample evaluation was done for several states of charge. the Figure S 2 shows the charge and discharge curves each sample performed in order to be at the SoC that it was evaluated.

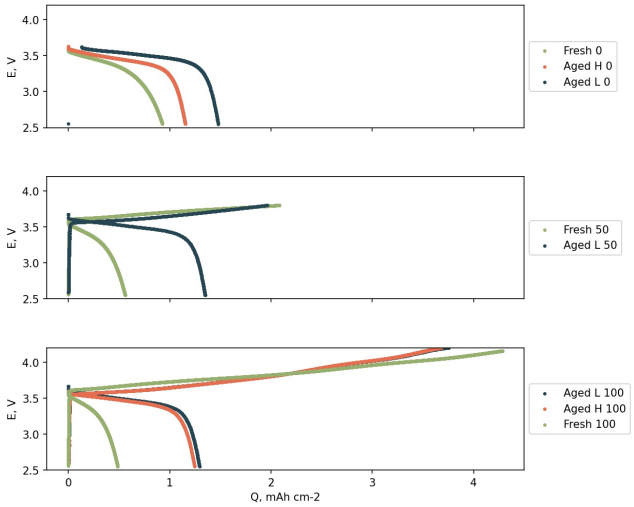

Figure S 2: Fresh, Aged L, and Aged H sample preparation

SEM

Figure S 3 shows SEM image of the particles of the Aged L electrode. Here, the secondary particles are $\sim$ 10 μm. The secondary particles are agglomerated primary particles with the average size $\sim$ 100 nm.

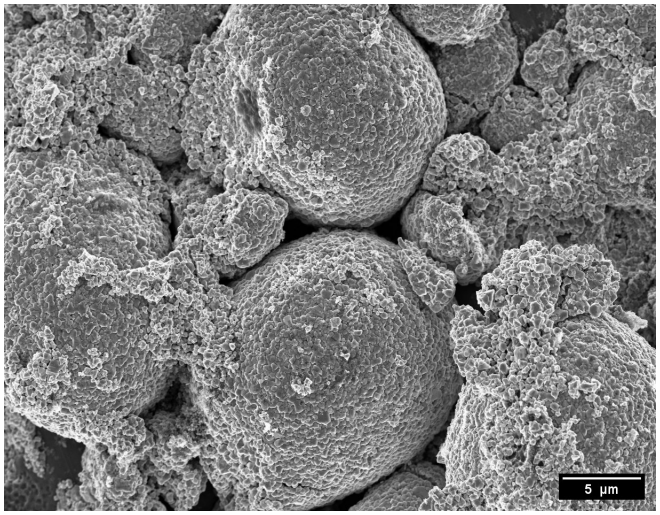

Figure S 3: SEM image of Aged L at 0%SoC.

EXAFS

The k^2-weighed $\chi(k)$ structures for Ni and Co (shown in Fig. S 4) supports EXAFS results with larger chemical shifts around Ni compared to Co on lithiation/delithiation, while for both TMs only small changes happen upon ageing. Fig. S 4 shows an overlay of the k^2-weighed $\chi(k)$ structures for Ni and Co ($\chi(k)^{\mathrm{Ni}}$; $\chi(k)^{\mathrm{Co}}$) from (a) fresh electrodes (dark yellow) in lithiated (Fresh 0) and delithiated (Fresh 100) states, (b) aged electrodes at low %SoC (dark blue) in lithiated (Aged L 0) and delithiated (Aged L 100) states, and (c) aged electrodes at high %SoCs (wine) in lithiated (Aged H 0) and delithiated (Aged H 100) states.$\chi(k)^{\mathrm{Co}}$ data was limited to $k_{max} \sim 12$ Å^{-1} by the presence of Ni in our samples and the $\chi(k)^{\mathrm{Ni}}$ data extended up to $k_{max} \sim 14$ Å^{-1}, establishing high crystallinity of the samples and high quality of acquired data. With increasing k, the frequency components of $\chi(k)^{\mathrm{Ni}}$ and $\chi(k)^{\mathrm{Co}}$ shifts towards larger wavenumbers upon delithiation. But only small changes happen upon ageing. The shifts are notably higher for $\chi(k)^{\mathrm{Ni}}$ compared to $\chi(k)^{\mathrm{Co}}$, consistent with a larger chemical shift for Ni. The overall $\chi(k)^{\mathrm{Ni}}$ reveals some major Fourier frequency components matching with $\chi(k)^{\mathrm{Co}}$, but with some minor components visibly different from $\chi(k)^{\mathrm{Co}}$. This indicates that while Ni and Co share the same crystallographic site

in the structure, the two metals adopt characteristic local environments, while still keeping the global periodicity intact. The differences between $\chi(k)^{Ni}$ at 0 and 100 % SoC appear larger as compared to the differences between $\chi(k)^{Co}$ at 0 and 100 %SoC, indicating that delithiation induces stronger changes in the local structure of Ni than Co. Interestingly, for a given electrode, the differences between $\chi(k)^{Ni}$ and $\chi(k)^{Co}$ is significant in the lithiated state, whereas in the delithiated state, these differences became more suppressed.

Fig.5 shows the corresponding pseudo Debye-Waller factors (σ^2), and the results clearly reveal that a disorder in the O-environment around Ni ($\sigma^2_{\text{Ni-O}}$) in the lithiated electrodes is significantly larger than Co ($\sigma^2_{\text{Co-O}}$). On the other hand, no appreciable changes were observed for the $\sigma^2_{\text{Co-O}}$ values. However, upon delithiation the $\sigma^2_{\text{Ni-O}}$ values abruptly drop, assuming values similar to $\sigma^2_{\text{Co-O}}$. Therefore the O_6 environments about Ni and Co assume similar descriptions upon delithiation, as already discussed in Fig. 5.

RIXS

By comparing the spectra of the 2.0 V and 4.8 V samples in Fig. 6, a first estimate for the amount of redox active oxygen can be made. For this, it is assumed that the Fresh NCA 2.55 V cathode carries no molecular oxygen or otherwise oxidized oxygen from the anionic redox process as it is fully delithiated. The change in the spectral weight when charging to 4.2 V is then ascribed to any redox active oxygen species. There are two prominent features found in Fig. 7. One at -7.7 eV associated with the formation of O_2, and a shoulder at roughly -4.8 eV believed to be a result of reversible lattice oxygen participation. The integrated area of the spectrum lower in energy than the vibrational peaks (-12 eV to -2 eV) can then be compared for both 2.55 V and 4.2 V spectra and the increase in the 4.2 V sample can be calculated. This results in an area increase of 12%, meaning an estimated 12% of the contained oxygen participates in the oxygen redox process. This can further be

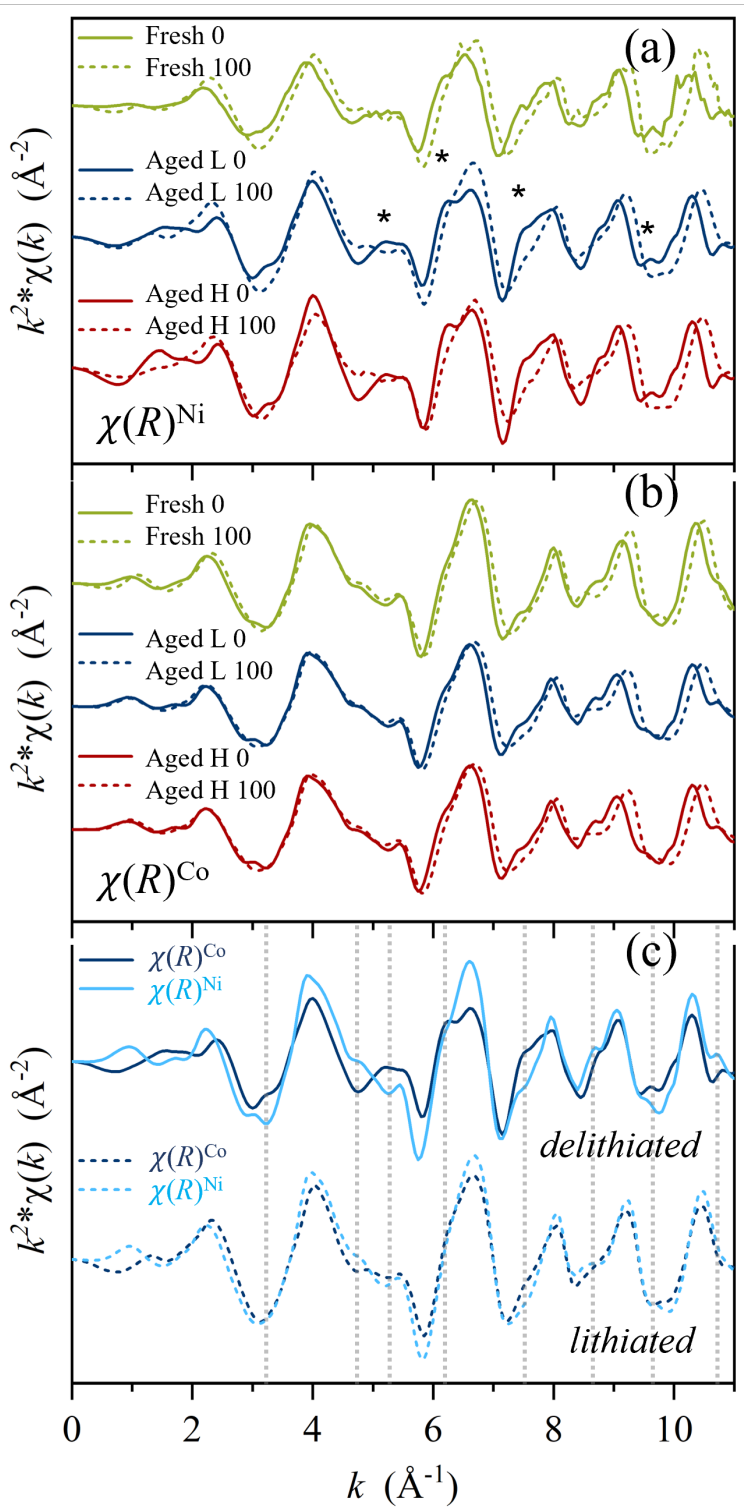

Figure S 4: k^2-weighed (a) $\chi(k)^{Ni}$ and (b) $\chi(k)^{Co}$ for fresh electrodes (dark yellow), aged electrodes at low potential (Aged L: dark blue) and high potential (Aged H: wine) in lithiated (0% SoC) and delithiated (100% SoC) conditions (c) Comparison of $\chi(k)^{Ni}$ and $\chi(k)^{Co}$ between lithiated and delitiated states for the Aged L electrode.

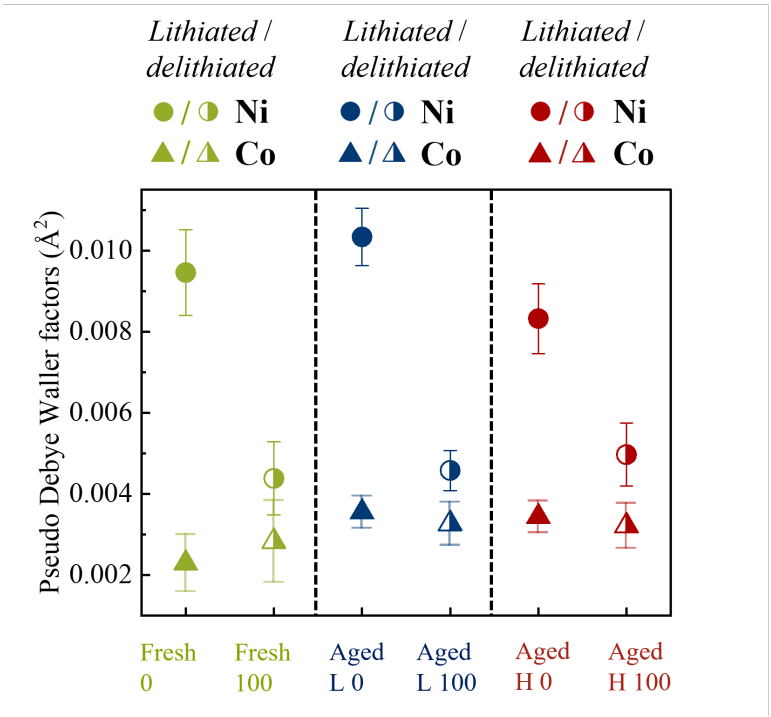

Figure S 5: Comparison of pseudo Debye-Waller factors from Ni (circles) and Co (triangles) sites in lithiated (filled symbols) and delithiated state (half-filled symbols) for fresh electrodes and electrodes under different ageing conditions.

analyzed by splitting the contributions of the formed molecular oxygen and the participating lattice oxygen using the area from the individual features at -7.7 eV and -4.8 eV. The area around both features is calculated after subtracting the scaled 2.55 V spectrum and compared to the full area of the 4.2 V sample. This results in an estimated contribution of 4.5% O_2 formation and 7.5% participation of lattice oxygen. Finally, this calculation should be treated as a rough estimate of the amount of redox active oxygen and thereof derived estimate for the amount of formed O_2.

The peak fitting was done by fitting the elastic peak and the first three vibrational peaks together for all samples in the integrated spectra over the excitation energies 531.2-533.2 eV. Calculating the area of the vibrational peaks then becomes independent of the contribution of the elastic peak. The ratio in peak area between the vibrational peaks of the fresh and the two aged samples then results in 46.8% and 41.1% for the Aged L and Aged H samples respectively.

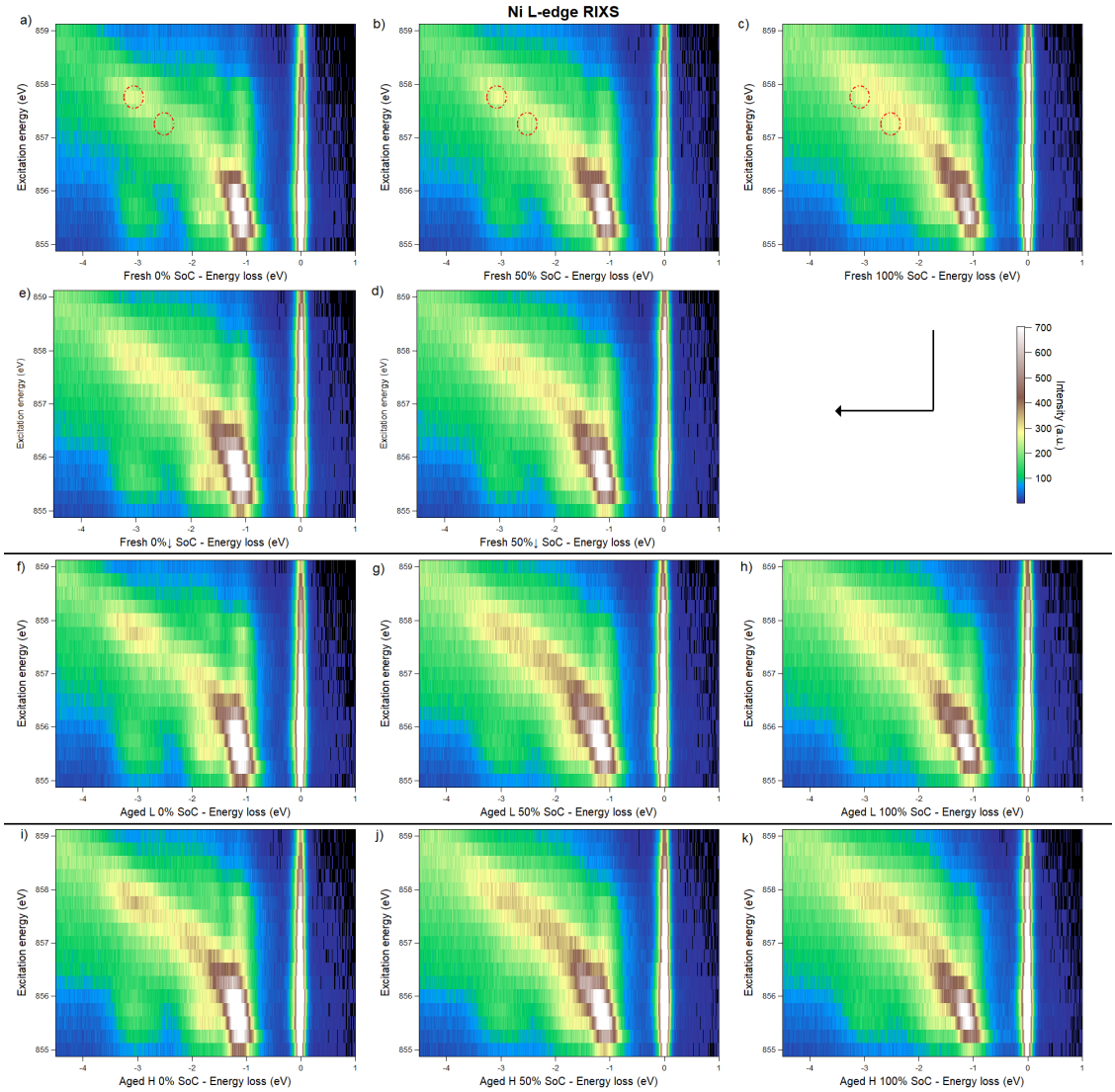

Figure S 6: Ni L-edge RIXS maps for all NCA samples starting from the top left with the Fresh samples (a-e), then the Aged L sample (f-h) and finally the Aged H samples (i-k). Red ovals signify areas of interest that could indicate changes in the oxidation state of Ni.

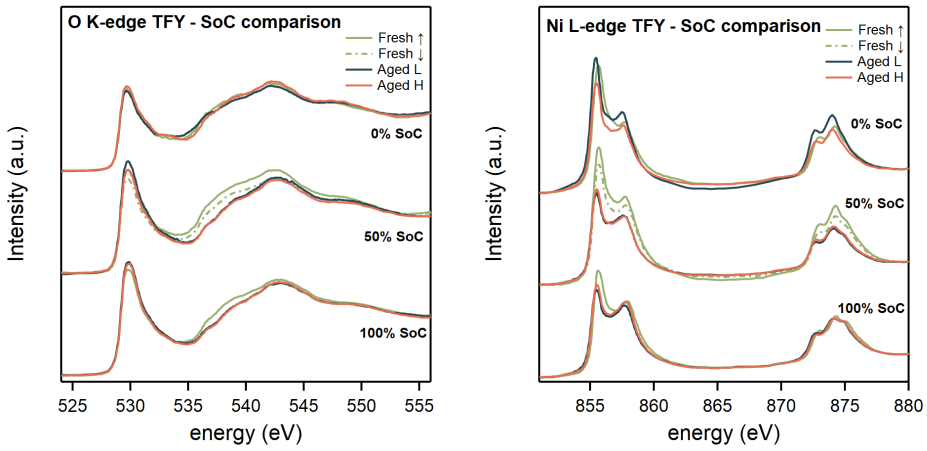

Figure S 7: O K- (left) and Ni L-edge XAS (right) spectra taken in TFY and arranged to compare samples of the same potential.

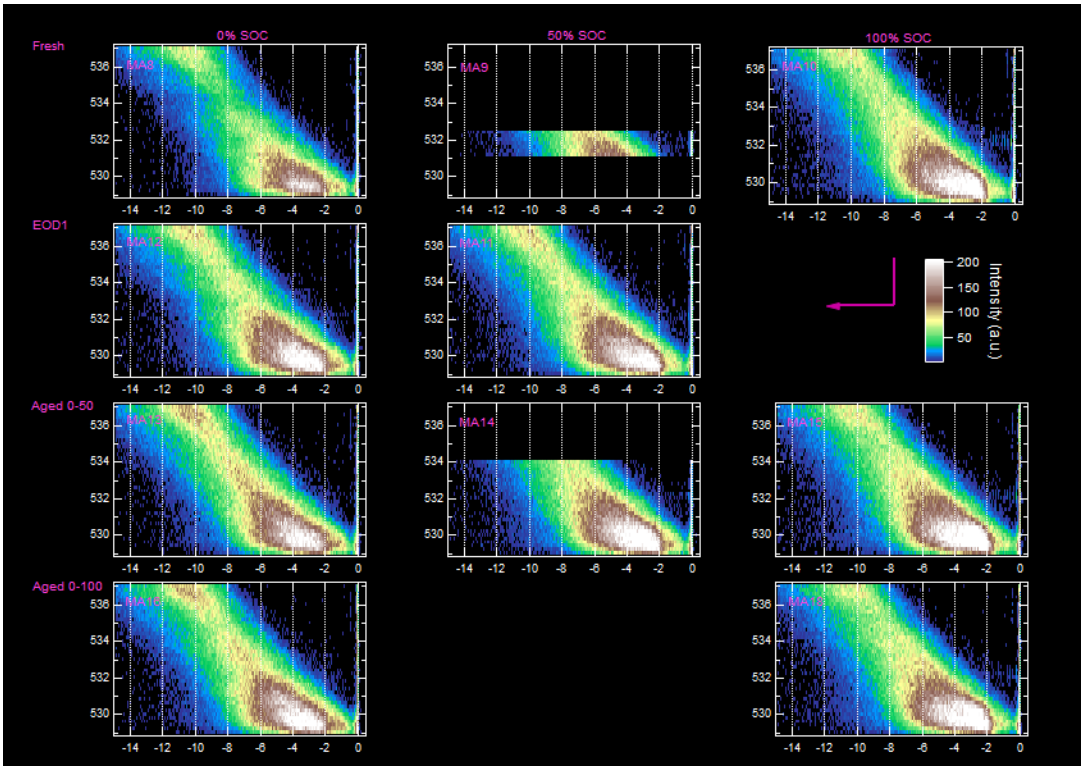

Figure S 8: Full O K-edge RIXS maps of all investigated samples.

The result from the O *K*-edge PFY in Fig. 9 is in agreement with the TFY data. There is an increase in the pre-edge area during charge and the fresh samples display minor changes when charging from 50 and 100% SoC. Comparing 0 and 100% SoC samples, the

pre-edge area increase is lower in the PFY compared to the TFY data, especially for the Aged H samples. However, this does not affect the overall conclusions of the O *K*-edge XAS data as the trends are consistent between the two. The reason for this difference is not certain, but, apart from other factors, it could arise from self-absorption. Previously,

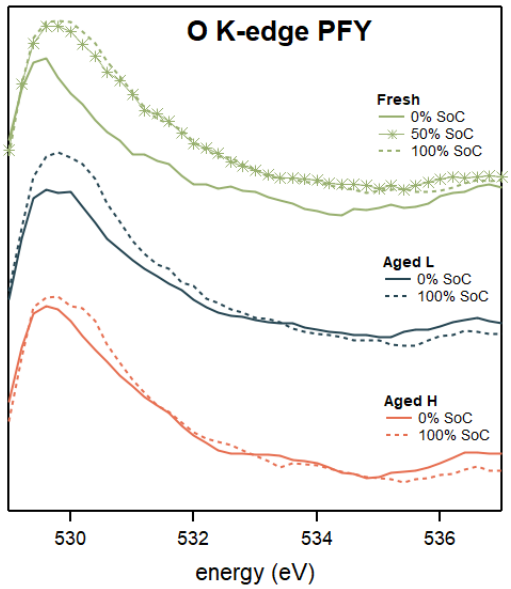

Figure S 9: O *K*-edge XAS spectra taken in PFY mode.

for Li-rich cathode materials, a vibrational O_2 feature has been observed in the RIXS maps at an excitation energy of approx. 531 eV upon charging to high voltages.[4] Additionally, a peak at approx. -7.5 eV energy loss appears in conjunction with the vibrational feature at the same excitation energy in the Li-rich cathodes. This peak is assigned to transitions to the $3\sigma_g^{-1}1\pi_g^{33}\Pi_g$ final state of molecular O_2 through the intermediate $1\sigma_g^{-1}1\pi_g^{33}\Pi_u$.[5] Fig. 10 illustrates the O *K*-edge RIXS spectra of the 0 and 100% SoC Fresh samples, with excitation energy of 532.2 eV. The emergence of both the O_2 vibrational and $1\sigma_g^{-1}1\pi_g^{33}\Pi_u \rightarrow 3\sigma_g^{-1}1\pi_g^{33}\Pi_g$ feature is visible for the NCA during charge. For reference, spectra of 2.0 V and 4.8 V Li-rich NMC are shown to compare the O_2 formation with the NCA. Furthermore, the spectrum for the 100% SoC Fresh sample in Fig. 10 exhibits another prominent feature centered around $\approx$ -4.8 eV. This region is tied to the charging of the NCA since the peak is

a consistent feature among all 100% SoC NCA samples while not being present in the 0% SoC samples. The origin of this intensity increase cannot be attributed to the formation of molecular oxygen.[5]

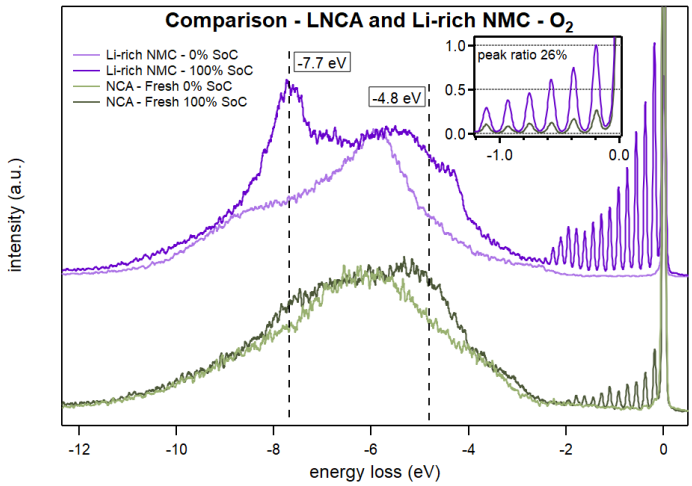

Figure S 10: O *K*-edge RIXS spectra displaying the region of O_2 vibrations corresponding to 532.2 eV excitation energy. Displayed are spectra of the 0 and 100% SoC Fresh NCA samples as well as 2.0 V and 4.8 V of a Li-rich NMC material. The feature at -7.7 eV corresponds to the energy loss peak found in free molecular oxygen. In the inset, the vibrational features of the two materials are compared for the NCA 4.2 V and NMC 4.8 V samples. In the first peak, the Fresh NCA sample reaches 26% maximum intensity of the Li-rich sample. The intensity of the 2.0 V spectra have been scaled until they barely overlap with the 4.8 V spectra for both materials providing a clearer picture of the changes that occur in this region during charge.

The measurements of the Ni *L*-edge can be seen in Fig. S 6 where one area at 857.25 eV incident energy and -2.5 eV energy loss displays significant change in intensity during cycling. The intensity of the area has been integrated and normalized to the integrated intensity of the area at 857.75 eV incident energy and -3.1 eV energy loss and is presented in Fig. 9, where the left panel shows O *K* pre-edge area Fig. 9 (a) and the right panel shows Ni *L*-RIXS peak ratio Fig. 9 (b) and the change in the ratio reflects a change in the redox activity. This area ratio could possibly be used as fingerprints to identify changes in oxidation state of the Ni during charging as the change in ratio consistently correlates

to the change from $Ni^{2+/3+}$ to more $Ni^{3+/4+}$-like characteristics. In case of O *K* pre-edge area, a clear increasing trend can be identified for both fresh and aged samples between 0 and 50% SoC (Fig. 9 a, left). When the delithiation continues further, the Fresh sample intensity ration remains the same whereas the aged samples shows a continued increasing trend, with Aged H showing a greater slope. As for the Ni *L*-RIXS peak ratio, a consistent intensity ratio decrease is observed for the full delithiation.The decrease for the Fresh samples appears more linear. The difference in the trends between 0-50 and 50-100 %SoC suggests difference in charge compensation rates where Ni in the aged sample have faster transition to higher oxidation states than in fresh electrodes. The complementary measurement in PFY is also shown in Figure S 11.

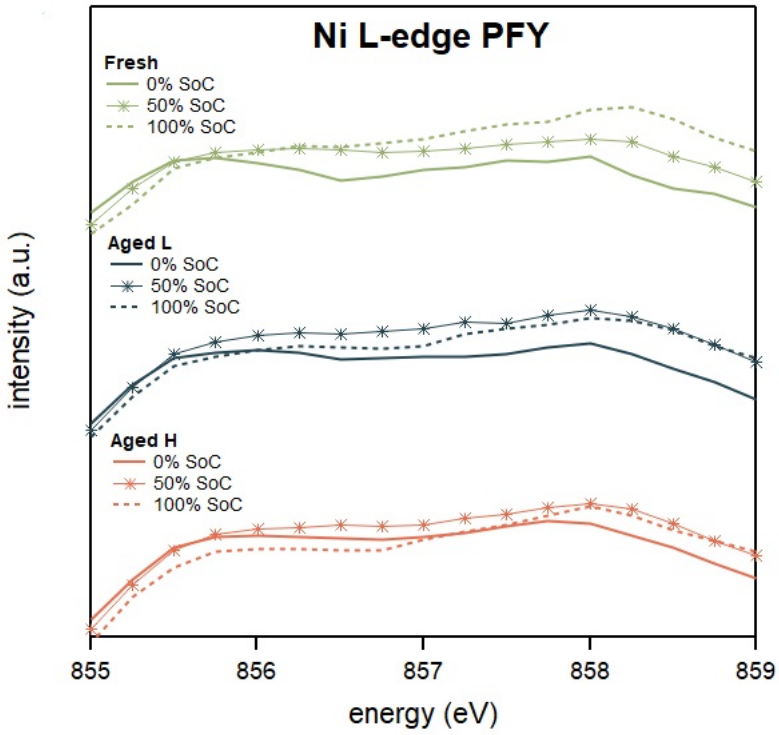

Figure S 11: Ni *L*-edge PFY.

HAXPES

Hard X-ray photoelectron spectroscopy (HAXPES) was used to perform more in-depth material characterization. HAXPES measurement were done using HAXPES Lab Scienta Omicron with Ga photon source, Scienta Omicron EW4000 analyzer and Basler AG MCP detector. The Fresh and Aged H (Table S 1) electrodes were used both as opened (0%SoC) and partially delithiated (100%SoC) states for the measurements. To address the changes occurring in the NCA material during its electrochemical activity, O 1*s* (Fig. S 12(a)), Ni 1*s* (Fig. S 12(c)), Ni 2*p* (Fig. S 12(d)) were studied. Comparison of Ni 1*s* (Fig. S 12(c)) and Ni 2*p* (Fig. S 12(d)) suggests that ageing effects on Ni differs for the surface and the bulk of the material. Additionally, Al 1s spectra was observed which shows two states of Al in the material. It might be related to the fact that the sample surface contains residues from ceramic coating of the separator (Al_2O_3 [1]) which can also bring contribution to the observed O 1s spectra (Fig. S 12(a)).

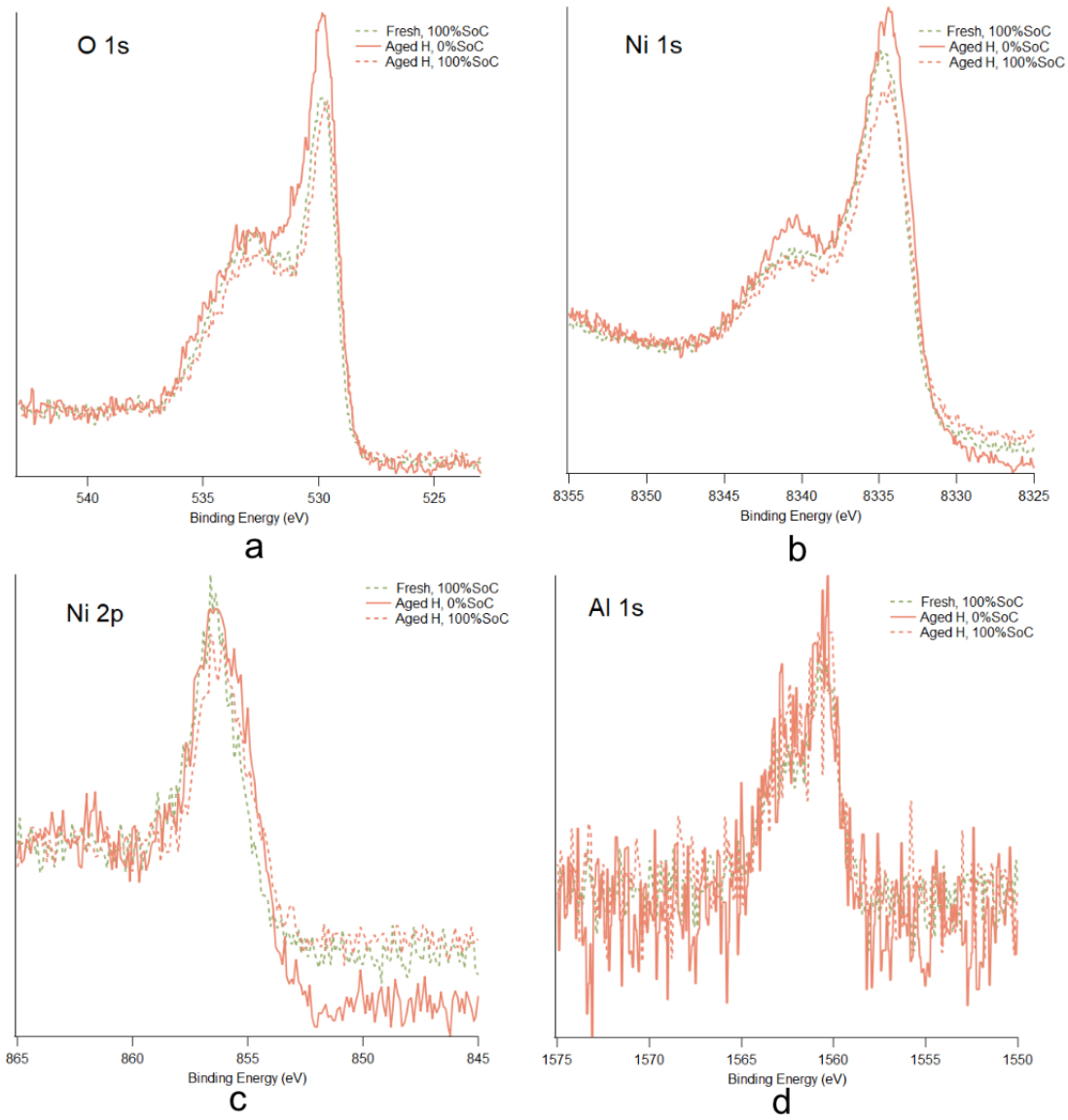

Figure S 12: Spectra of Fresh and Aged L samples collected using HAXPES: O 1*s* (a), Al 1*s* (b), Ni 2*p* (c) and Ni 1*s* (d).

References

(1) Mikheenkova, A.; Smith, A. J.; Frenander, K. B.; Tesfamhret, Y.; Chowdhury, N. R.; Tai, C.-W.; Thiringer, T.; Lindström, R. W.; Hahlin, M.; Lacey, M. J. Ageing of High Energy Density Automotive Li-ion Batteries: The Effect of Temperature and State-of-Charge. 2023; https://chemrxiv.org/engage/chemrxiv/

article-details/6448f6d783fa35f8f6466c8c.

(2) Mikheenkova, A.; Gustafsson, O.; Misiewicz, C.; Brant, W. R.; Hahlin, M.; Lacey, M. J. Resolving high potential structural deterioration in Ni-rich layered cathode materials for lithium-ion batteries operando. *Journal of Energy Storage* **2023**, *57*, 106211.

(3) Ravel, B.; Newville, M. ATHENA, ARTEMIS, HEPHAESTUS: data analysis for X-ray absorption spectroscopy using IFEFFIT. *Journal of Synchrotron Radiation* **2005**, *12*, 537–541, Number: 4 Publisher: International Union of Crystallography.

(4) Sharpe, R.; House, R. A.; Clarke, M. J.; Förstermann, D.; Marie, J.-J.; Cibin, G.; Zhou, K.-J.; Playford, H. Y.; Bruce, P. G.; Islam, M. S. Redox Chemistry and the Role of Trapped Molecular O2 in Li-Rich Disordered Rocksalt Oxyfluoride Cathodes. *J. Am. Chem. Soc.* **2020**, *142*, 21799–21809.

(5) Glans, P.; Gunnelin, K.; Skytt, P.; Guo, J.-H.; Wassdahl, N.; Nordgren, J.; Ågren, H.; Gel'mukhanov, F. Kh.; Warwick, T.; Rotenberg, E. Resonant X-Ray Emission Spectroscopy of Molecular Oxygen. *Phys. Rev. Lett.* **1996**, *76*, 2448–2451.